Stabiliser Free, Low Solvent Waste Exfoliation of 2D-materials for Printed Memristors

Jinrui Chen[1,3], Nasiruddin Macadam[1,3], Mingfei Xiao[1,3], Tynee Bhowmick[1], Binghan Zhou[1], Zhuo Chen[1], Abrar Alhazmi[1], Shaoliang Guan[2], Georgios Psaltakis[1], Osarenkhoe Ogbeide[1], and Tawfique Hasan[1,4,5,*]

[1]Cambridge Graphene Centre, University of Cambridge, 9 JJ Thomson Avenue, Cambridge, CB3 0FA, UK
[2]Maxwell Centre, Cavendish Laboratory, University of Cambridge, Cambridge, CB3 0HE
[3]Equal contribution to the work
[4]Senior author
[5]Lead contact
[*]Correspondence: th270@cam.ac.uk

SUMMARY

Conventional exfoliation relies on stabilizers or harsh solvents, limiting scalability and requiring post-processing. We present a low waste, stabilizer-free method for exfoliating 2D materials using high pressure homogenization (HPH) in isopropyl alcohol (IPA). We optimize HPH with MoS_2 and benchmark it against ultrasound-assisted liquid phase exfoliation (LPE) method. The optimized HPH process achieves a 20% yield, significantly higher than the 1.2% yield of LPE, while generating only 10% of the solvent waste. Life cycle assessment (LCA) confirms the lower environmental footprint of HPH. We further demonstrate this method's applicability to other layered materials. To evaluate the suitability of exfoliated materials for printed device fabrication, we formulate HPH-exfoliated MoS_2 ink and fabricate inkjet-printed memristors, which show enhanced performance and reduced variability compared to LPE-based devices. These results highlight the advantages of HPH in producing high quality 2D materials ink with reduced environmental impact and better processability for scalable printed electronics.

KEYWORDS

High Pressure Homogenization, Liquid Phase Exfoliation, Inkjet Printing, Memristor, Printed Electronics, Sustainability

INTRODUCTION

Solution-based exfoliation of 2D-materials is established as the method with the most potential to obtain mono-/few-layer nanoflakes from bulk crystals on a large scale. This is because these methods are low-cost, more easily scaled and faster when compared to others, such as mechanical exfoliation[1] and even bottom-up approaches such as chemical vapour deposition[2]. The quality of the exfoliated material is often compromised but is still sufficient for use in a wide range of applications, including in electronics[3–5], photonics[5–7] and sensing[8,9]. The key advantage of solution-based exfoliation is that it facilitates formulation into inks[10], which can be deposited on a wide range of flexible substrates by employing mature printing methods[11]. This enables the whole process, from bulk nanomaterial to exfoliated nanoflakes in devices, to be scaled up.

Solution-based exfoliation can take many forms, most notably chemically-assisted[12], molecule intercalation-assisted[13,14], ball milling[15], shear mixing[16], electrochemical exfoliation[17] and ultrasound-assisted[18–20] processes, which are all capable of exfoliating large amounts of material. However,

despite the possibility of solvent recovery in principle[21], conventional solution-based exfoliation methods often involve significant solvent loss during solvent exchange, centrifugation, and purification steps. These wastes can take the form of surfactant/polymer stabilisers which play no role in the final deposited material and can even hinder the desired performance[11]. They can also take the form of reactive acids/oxidants or particularly harsh solvents such as N-methyl-2-pyrrolidone (NMP), all of which complicates the scaling up of such processes. In the literature, the type and the amount of waste are not usually considered, especially when the yield of such exfoliation methods is reported, with only the unexfoliated material considered waste. However, to get a true representation of the efficiency of an exfoliation process, the amount of the starting materials, including solvents used in various stages of these processes must be considered. We have coined this term as the 'process yield' which offers a clearer understanding of the amount of waste associated with a certain exfoliation technique. In turn, this allows a more valid evaluation of the process which becomes significantly more apparent when scaled to commercial levels.

The most commonly reported solution-based exfoliation technique is ultrasound-assisted liquid phase exfoliation, which we will hereon refer to as LPE. This is most frequently conducted using an ultrasonic bath and has been demonstrated for a plethora of 2D-materials[5,13,18]. The basic principle of the technique is to exfoliate atomically thin flakes from the bulk by shear forces generated by the collapsing bubbles created by ultrasound in a liquid medium. This is typically a pure or mixed solvent system with favourable interaction with the 2D material (matching Hansen solubility parameters)[13] or may contain surfactants or polymers to stabilise the exfoliated flakes.

By optimizing ultrasonication protocols and selecting suitable stabilizers, several LPE studies have achieved excellent exfoliation efficiencies. For instance, the use of bovine serum albumin (BSA) as a bio-surfactant enabled a MoS_2 exfoliation yield of up to 27.2%[22], while natural saponin-based surfactants have been shown to achieve a 33% yield for h-BN[21]. In addition, aromatic dispersants such as bis-pyrene derivatives have demonstrated strong stabilizing capabilities[23], promoting long-term colloidal stability of exfoliated nanoflakes in aqueous media.

Despite these advances, LPE still faces several intrinsic limitations. High-yield protocols typically require prolonged sonication times, which may range from several hours to days, resulting in low throughput and high energy consumption. More critically, these methods often rely on surfactants or stabilizing agents that are difficult to fully remove after exfoliation (see Table S1). When stabilising agents are used, they can interfere with the performance of the final deposited material[11]. Therefore, they are commonly removed or burned off through thermal annealing[24]. However, this process is not viable for many flexible substrates that cannot tolerate temperatures substantially above 100 ℃. As a result, many researchers have turned to solvents with more closely matched Hansen solubility parameters to avoid the use of stabilisers[25]. These solvents often take the form of harsh, toxic, high boiling point (BP) solvents such as NMP and dimethylformamide (DMF), which are typically exchanged in later stages for lower BP solvents to facilitate material processing and deposition. Yet, this solvent exchange step adds cost and complexity and introduces additional solvent waste, leading to a larger environmental footprint. Although studies have employed IPA or water as exfoliation agents to produce 2D materials (see Table S2), challenges such as low process yield, poor solvent utilization, and prolonged processing time remain unresolved.

The inefficiency of the LPE method can be attributed to the non-uniform distribution of ultrasound through the sample. For bath sonication, the intensity is low and more concentrated around the ultrasonic transducers[26,27] whereas for tip sonication, the initially high intensity exponentially decays as we move away from the tip[28]. Therefore the material is not uniformly exposed to the exfoliating shear forces. A similar non-uniform exposure to shear forces is seen in the high shear mixing technique, where it peaks in the gap between the stator and the rotor[29,30]. This was overcome by Ref.[31] which demonstrated a sodium deoxycholate (SDC) assisted, graphite exfoliation *via* an in-line cyclic high-shear mixing system. This periodically subjects the entirety of the

sample to shear forces, vastly improving the yield weight (Y_w, ratio of dispersed material mass and initial mass) and throughput (ϕ, mass exfoliated per hour). As this process can be up-scaled easily, this is a huge step towards achieving efficient, larger scale exfoliation of 2D-materials.

High-pressure homogenisation (HPH) through microfluidisation is a promising technique as it is inherently cyclic, allowing the application of high shear forces across the entirety of a sample. In this process, a material is homogenised and dispersed by forcing it through microchannels (87 μm - 200 μm) under high pressure. This technique has been demonstrated for the exfoliation and dispersion of nanomaterials[32–34]. In particular, high concentration (up to 100 g.L^{-1}) graphene dispersions have been reported with a Y_w, = 100 % using carboxymethyl cellulose (CMC) sodium salt as a stabiliser,[33] demonstrating the viability of this strategy as an efficient, scalable exfoliation of graphite in water.

However, there has been little to no investigation for other 2D materials. More importantly, stabiliser-free exfoliation of any 2D material directly in pure solvents has never been considered. Herein we present a stabiliser-free exfoliation and dispersion of MoS_2 *via* HPH directly in IPA, a biocompatible[35] and low-cost solvent which is commonly used in the laboratory and lends itself to simple formulation into inkjet printable inks[5]. We evaluate the key metrics of this exfoliation alongside ultrasound-assisted LPE, starting with the same amount of 2D material powders (small crystals) and initial concentration to allow for a direct comparison. Memristors have emerged as promising components for next-generation storage and neuromorphic computing due to their non-volatility, high density, and low power consumption[36]. 2D materials, with their unique layered structure and tunable electrical properties, enable low-power operation and high-density integration in 2D material-based memristors.[37,38] The performance of memristors is highly dependent on the size, uniformity and vacancies of the 2D materials used as the switching layer.[37] To evaluate the impact of different exfoliation methods on printed device performance, we use inkjet printing to fabricate memristors from MoS_2 nanoflakes obtained via both HPH and LPE methods. We also compare HPH and LPE exfoliation methods with a range of other 2D-materials ($MoSe_2$, *h*-BN, In_2Se_3 and Bi_2Te_3) to allow for a more rounded evaluation of their exfoliation ability, highlighting the clear overall advantages of HPH.

RESULTS and DISCUSSION

Optimization of HPH Parameters for MoS_2

Based on previously reported microfluidisation of graphite[33,34], we begin the optimisation of the MoS_2 dispersion. A key difference in our process is the absence of a stabiliser, allowing for the final product to consist solely of the material and solvent, mitigating the need for the additional stabiliser removal step. The HPH system we use is schematically depicted in Figure 1A. The process involves the preparation of a mixture of solvent and the starting material to be exfoliated. A high pressure pump draws in this mixture and forces it through a microchannel (87 μm). This process generates intense mechanical forces, including high shear rates, turbulence, and cavitation effects, which are crucial for effective exfoliation of layered materials. The rapid acceleration through the microchannel produces high shear rates, generating sufficient stress to overcome the van der Waals forces binding the layers[30,39]. Additionally, turbulent flow enhances particle mixing and collisions, further facilitating exfoliation[40]. Rapid pressure fluctuations also trigger cavitation, where microbubbles form and collapse violently, producing localized shockwaves that assist in layer separation[41]. These combined forces enable efficient delamination of bulk materials into few-layer nanoflakes without stabilising agents, thereby preserving the intrinsic properties of the 2D materials. The mixture then passes through a second channel (200 μm) which acts as a pressure backdrop. In this wider channel, the sudden expansion and corresponding

pressure drop help stabilize the flow and reduce the temperature rise induced by high-pressure processing. Additionally, the abrupt change in channel size can further enhance turbulence and promote the formation of microjets and shockwaves. These phenomena contribute to additional mechanical disruption of the layered structure, thereby assisting in the delamination process. It then passes through to a condenser to dissipate the heat generated due to the high pressure processing. The material at the outlet can be collected or fed directly back into the inlet for the next cycle. Multiple cycles enhance the exfoliation efficiency, ensuring that the entire sample undergoes sufficient mechanical processing to achieve uniform nanoflake production.

Our HPH process (outlined in Figure S1) begins by mixing powdered 2D material crystal into IPA. It is a widely used, inexpensive, low boiling point solvent and has been exploited for 2D-material ink formulations[5,6,42–51]. IPA is also safer to handle and easier to dispose of in comparison to other commonly used solvents for LPE such as NMP and DMF. The crystal-IPA mixture is processed through the HPH for the desired number of cycles and once collected, is centrifuged at low speed to remove any unexfoliated material; see Experimental section for details.

For this study, we first optimise the initial concentration of powdered crystal-MoS_2 (PC-MoS_2), by establishing a suitable compromise between the concentration and the yield (Y_w) of the resulting dispersions. The Y_w accounts for the efficiency of the exfoliation, taking into account the initial mass of PC-material and the amount of material dispersed in the final product. We process all samples (with 2.5-12.5 mg.mL^{-1} PC-MoS_2 concentration) for 150 cycles and centrifuge them under the same conditions to separate unexfoliated materials. Figure 1B shows the UV/Vis absorption spectra from these samples and the corresponding estimated concentration. For this, we use the Lambert-Beer law, $A = \alpha_\lambda cl$, where A is the absorbance, c is the concentration (g.L^{-1}), l is the path length (m) and α_λ is the extinction coefficient at wavelength λ[13,18]. We use α_{345} = 6820 L.g^{-1}.m^{-1} [52,53] as it lies in the region of the spectrum that has the lowest contribution from scattering, which varies according to the size and thickness of the flakes in the dispersion. We find a consistent increase in the final concentration as the initial amount of PC-MoS_2 is increased, except for 12.5 mg.mL^{-1} which shows a considerably smaller increase. We believe this is due to the capacity saturation of the IPA to disperse MoS_2 without stabilisers. With only a marginal increase in the concentration and significant decrease in the percentage of the initial PC-MoS_2 in the final dispersion for the 12.5 mg.mL^{-1} (Figure 1D(i)), we conclude that the 10 mg.mL^{-1} is the optimal initial concentration for stabiliser-free dispersion of MoS_2 via HPH.

An imperative process parameter for HPH that dictates both material properties and the time taken to exfoliate is the number of cycles the mixture is processed. We probe this by using the optimised 10 mg.mL^{-1} initial concentration mixtures and cycling for 50-250 cycles (50c - 250c). Using the UV/Vis data displayed in Figure 1C, we see that the concentration of the resulting dispersion increases with an increasing number of cycles. We see a plateau in the final concentration between 200c-250c as observed between the initial concentrations of 10 mg.mL^{-1} - 12.5 mg.mL^{-1}. For our HPH process, the rate of processing is 26.6 L.h^{-1}. Assuming we are processing 1 L, 50 cycles would amount to $\sim$2 hours of additional processing time for 250c. Factoring this, we consider 200 cycles a suitable compromise between the time taken and the yielded dispersion concentration. Also, as seen in Figure 1D(ii), the percentage Y_w increase every 50 cycles gets smaller with increasing number of cycles. It is a 4.49 % increase from 50c-100c, 3.29 % increase from 100c-150c, 2.97 % increase from 150c-200c and 1.17 % increase from 200c-250c. Although any increase in Y_w is desirable, we deem the added time more important when compared to 200c. We therefore consider 200c an optimal number of cycles for the stabiliser-free dispersion of MoS_2 using HPH.

The Y_w for 10 mg.mL^{-1} initial concentration for 200c is 17 %. This is relatively high when compared to other solution-based exfoliation of MoS_2 (< 5 %)[13,15,54]. However there is still a considerable amount of MoS_2 sediment that is collected during centrifugation. To determine if

the unexfoliated material could be reused, we collect the sediment after centrifugation and reprocess the material with an initial concentration of 10mg.mL^{-1} for 50c-200c. The characterisation of these "recollected" HPH samples is shown in Figure S2. We find that 200c yields the highest concentration of all the recollected samples, but it is lower than the concentration yielded from the original process. The Y_w for 200c recollected HPH sample is 13.4 % compared to 17 % for the original dispersion. We believe this is a result of the material already being partially exfoliated/deagglomerated from the first round of HPH, leading to a lower proportion of bulk MoS_2 which is more readily exfoliated. This is supported by the lower increase in Y_w between 50c-100c for the recollected dispersion, 2.2 % increase, in comparison to 4.49 % increase in the original HPH trial. We suggest that the lower Y_w for the recollected dispersion could potentially be improved by increasing the initial concentration or with a greater number of cycles. Nonetheless, recollecting the unexfoliated material and processing it through the HPH for a second time provides a path to reduce the amount of waste from the initial process and has the potential for further recollection and waste reduction.

The concentration of the dispersions cannot be used as the sole metric to optimise the exfoliation process, the material properties must also be evaluated. We probe the flake height and lateral dimensions using atomic force microscopy (AFM), with the results for the varying number of cycles shown in Figure 1E. The mean flake height is consistently around 3 nm, corresponding to approximately 4–5 MoS_2 layers. However, the variation of the flake height decreases considerably with increased cycling. It is clear that the average flake lateral size and the distribution decreases with a greater number of cycles, 85 nm $\pm$ 66 nm, 75 nm $\pm$ 41 nm, 67 nm $\pm$ 30 nm, 64 nm $\pm$ 25 nm, and finally 53 nm $\pm$ 22 nm from 50-250 cycles, respectively. From this data, we conclude that 150c-200c is a suitable number of cycling, as we find further processing starts to reduce the size of the already dispersed flakes without a justifiably large corresponding improvement in the homogeneity of the dispersion.

We also probe the recollected-MoS_2 samples with AFM to evaluate the properties of the recycled MoS_2 (Figure S2C). We find that the mean flake height shows a similar trend to the original HPH sample, while exhibiting smaller variation. The average lateral size also shows a similar trend, with an average flake size of 72 nm $\pm$ 41 nm, 56 nm $\pm$ 31 nm, 54 nm $\pm$ 22 nm, and 44 nm $\pm$ 16 nm from 50-200 cycles, respectively. For the recollected sample, we find that the significant drop in lateral size occurs at 200c, with the flakes already relatively small for the 100c and 150c samples. Despite taking into consideration the Y_w and concentration, the optimal number of cycles for the recollected MoS_2 is therefore 100c-150c. Optimisation of the exfoliation of recollected MoS_2 is beyond the scope of this work. However, a natural next step would be to increase the initial concentration and process for fewer cycles, to try and improve the Y_w without considerably reducing the average size of the flakes. Therefore, it is possible to utilise the unexfoliated MoS_2 from first round of HPH cycling through recollection and processing. This provides a pathway to make the HPH process more efficient, especially when scaling up is considered.

Benchmarking HPH Against LPE

To evaluate the viability of HPH as a stabiliser-free exfoliation technique, it must be compared to other established methods. Ultrasound-assisted LPE is the most commonly reported strategy for 2D material exfoliation[5,6,11]. We use a previously developed, tried and tested LPE protocol to achieve stabiliser-free dispersions in IPA. However, ultrasonication of 2D-materials directly in IPA yields little to no exfoliation without a stabiliser. We therefore first exfoliate the powdered crystals in NMP, with better matched Hansen solubility parameters, followed by a solvent exchange into IPA to yield the final dispersion (Process outlined in Figure S1). Such solvent exchange protocol

is a widely used strategy to obtain stabiliser-free dispersions in printing-friendly solvents[5,6,55–57]. Fourier Transform Infrared (FTIR) spectroscopy confirms the effective removal of NMP from the LPE MoS_2 sample following solvent exchange. As shown in Figure S3, the LPE sample (red curve) exhibits no detectable absorption at ~ 1665 cm^{-1} and ~ 1295 cm^{-1}, which correspond to the characteristic C=O and C–N stretching vibrations of NMP, respectively.[58] We then design an experiment to allow a direct comparison between the two exfoliation methods by starting with the same amount (2 g) of powdered MoS_2 crystals (Figure 2A) and 200 mL of starting solvent. For the HPH process, this is in a single container, while for LPE, this is split equally over 5 sonication vials for optimised exfoliation. We depict the dispersion at different stages of the processing, outlining the products that move forward in the process and highlight solvents that are discarded during the exfoliation of MoS_2 for HPH (Figure 2B) and LPE (Figure 2C) (See Figure S1 for a more complete process breakdown). This confirms considerably more waste for the LPE exfoliation of MoS_2. However, to get a better comparison of the processes, we continue to evaluate the differences by characterising the materials obtained.

We first characterise the material yielded from HPH and LPE by UV/Vis spectroscopy to allow for an estimation of the concentration in the dispersions. In Figure 2D, the characteristic spectrum for MoS_2 is observed for both dispersions with Abs_{345} being very similar. This is by design, due to the nature of the final steps of the LPE process, we are able to concentrate the LPE sample and bring it closer to the concentration yielded from the HPH exfoliation. We estimate the concentrations of the HPH sample to be 2.52 mg.mL^{-1} and the LPE sample to be 2.42 mg.mL^{-1}. The differences in the two spectra are the result of varying size and thickness properties of the flakes within the dispersions[53]. The sharper peaks of the HPH sample suggest more mono-disperse flake properties. Peak-A for the HPH sample is blue shifted which suggests presence of smaller and thinner flakes. By yielding inks with similar concentrations, we are able to make more direct comparisons of the two processes.

The HPH- and LPE-MoS_2 are compared using six different metrics, displayed in the radar plot in Figure 2E. These metrics encompass key factors for effective exfoliation of 2D materials and are explained as follows. (i) Concentration: How much material is exfoliated and stabilised in the final dispersion after centrifugation. (ii) Production rate: Volume of dispersion that is produced within a certain period of time. (iii) Yield weight: Y_w, is ratio of dispersed material mass and initial mass of PC-material input. (iv) Process yield: A value that better evaluates the efficiency of the exfoliation process by taking into account the complete dispersion yielded and evaluating it against all of the input. It is the percentage value of the mass of the final dispersion over the entire mass of the input PC-material and all of the solvent used during the process. (v) Percentage solvent discarded: Assesses the amount of solvent that is discarded (A) as a percentage of the total amount of solvent used in the entire process (B) to obtain the dispersion. The equation for percentage solvent discarded can be expressed as follows: $\frac{A}{B} \times 100$. Note that this is the only metric where a lower value is desired. (vi) Volume obtained: This shows the amount of dispersion obtained from the process with a starting volume of 200 mL.

The HPH dispersion is superior in every metric, except concentration where it is matched by design. Both the HPH and LPE uses bench top systems and are of comparable dimensions. The dispersion production rate (or throughput) is much higher for HPH (160 mL in $\sim$160 min) than for LPE (10 mL in $\sim$1000 min). This indicates that the process is faster. The Y_w for LPE is 1.2 %, compared to close to 20 % for the HPH. This does not consider potential for further improvement, as shown through successful dispersion of recollected MoS_2 by HPH, Figure S2. The proportion of solvent discarded in the processes are $\sim$97 % for LPE and 20 % for HPH, indicating a much greater efficiency of solvent utilisation. The process yield takes into account all of the reagents used and is 2.2 % for the LPE dispersion and 79 % for the HPH process. From these values, it is clear that the HPH process is considerably more efficient at utilising the input materials (PC-MoS_2 and solvent) and hence is less wasteful. In addition, HPH exfoliation of MoS_2 is faster,

has a higher throughput and is more efficient than the analogous binder-free LPE process; see Figure 2E. This coupled with the simpler procedure or HPH exfoliation with fewer steps (Figure S1) and avoidance of harsh solvents (NMP) make the process more scalable. To quantify the sustainability and environmental impact of LPE and HPH, we conduct a Life Cycle Assessment (LCA) study. LCA is a systematic tool for evaluating the environmental impacts of a product or service throughout its life cycle. It provides a basis for improving sustainability. Recognised under the ISO 14040 series, this methodology is standardised with principles and guidelines detailed in ISO 14040:2006[59] and ISO 14044:2006[60]. In this study, we adopt a gate-to-gate approach, focusing on the exfoliation process of MoS_2. The scope includes all steps from the beginning of the exfoliation process to the point where 2D MoS_2 is obtained, covering solvent usage and waste disposal. Hazardous waste incineration of spent solvents is also considered within the system boundaries. However, the upstream production of chemicals (e.g., MoS_2 powders, IPA, NMP) and the downstream application are excluded. The results show that the HPH method significantly outperforms LPE in terms of sustainability, with a carbon footprint that is 73.6% lower per batch and 98.4% lower per gram of product (See Supplementary Note 1).

One key consideration when contemplating large scale exfoliation of 2D-materials is the stability of the resulting dispersion. This is because unstable inks are usually unsuitable for printing and coating as large aggregates lead to printing issues such as nozzle clogging. The issues are compounded with poor material distribution in the printed pattern which can have adverse effects on the performance. We therefore evaluate the stability of the HPH and LPE MoS_2 dispersions. In undisturbed dispersions, material concentrations can be used as a means to evaluate their stability as material sedimentation progresses over time. To conduct this test, 5 mL of each dispersion is isolated and kept in vials which remained undisturbed for the duration of the test. On each day, 100 μL of dispersion was carefully removed from the top of the dispersion and diluted by a factor of 100, and the UV/Vis spectrum is measured. On the eighth day, the samples are subjected to vortex mixing (1 min) and ultrasonication (3 min) and a final UV/Vis measurement is collected. The results from the stability test are shown in Figure 2F. Through the change in measured concentrations, we observe faster sedimentation for the HPH sample over the seven day period. Under the same initial mass concentration, the smaller and thinner MoS_2 nanoflakes in the HPH sample exhibit a higher number concentration per unit volume, leading to an increased collision frequency and aggregation rate[61], thereby accelerating the sedimentation process. However, by day seven, we observe almost complete sedimentation of both the samples. Note that without stabilisers, this is expected in unfunctionalised 2D material dispersions in IPA.

The true indication of long term use of the dispersion is the ease of re-dispersion of the sediment. This property is critical in practical applications where storage and re-use of large-volume dispersions are required. We find that upon mild vortex mixing and short sonication, the concentration of the LPE sample is lower than the starting point, indicating partial irreversible sedimentation. For the HPH sample, the concentration increases, which is explained by the re-dispersion of the sediment at the bottom of the vial into the remaining solvent. At the end of the test there is 4.2 mL of the original 5 mL of dispersion remaining after small amounts of the dispersion are taken, diluted and measured throughout the test. According to DLVO Theory[62], the smaller size of MoS_2 nanoflakes in HPH samples results in weaker van der Waals forces due to reduced inter-flake surface contact area. This makes the formed aggregates more easily re-dispersible under vortex mixing and ultrasonic treatment. Therefore, the HPH sample lends itself more to large scale production of dispersions, as mild agitation is sufficient to re-establish the dispersion. This in turn allows for the dispersion to have a longer shelf life, which is required, especially for larger volumes of dispersions where they are unlikely to be used instantly. The need for more thorough agitation to attempt to re-establish the LPE dispersion signifies the formation of larger agglomerates which are more likely to cause issues further in the printing/deposition

process.

Extending HPH to Diverse 2D Layered Materials

We conduct stabiliser free HPH exfoliation of other 2D-materials ($MoSe_2$, *h*-BN, In_2Se_3 and Bi_2Te_3) to demonstrate the versatility of the method and compare the observations made between HPH and LPE exfoliation of MoS_2. The comparison summary of these dispersions is presented in Figure 3, with the UV/Vis spectra Figure S4. Figure 3A shows five radar plots, all comparing the same metrics used for the comparison of HPH and LPE for the materials tested. Similar trends that are seen for the exfoliation of MoS_2 (Figure 2E) by HPH and LPE are seen across all of the other materials.

The evaluation of the metrics for $MoSe_2$ and *h*-BN concur with the notion that HPH is a superior exfoliation technique. For $MoSe_2$, the key observations are the Y_w and the volume of dispersion obtained for the LPE sample, which are 5.4 % and 36 mL, respectively. These are better in relation to LPE-MoS_2, but still inferior to the HPH-$MoSe_2$. The *h*-BN dispersion *via* LPE produces the largest volume ($\sim$100 mL) of all LPE samples, leading to the best values observed for the other metrics for an LPE sample. Namely, Y_w ($\sim$15 %), process yield ($\sim$18.3 %), and percentage solvent discarded ($\sim$80 %). Despite this, the HPH counterpart is superior with a larger volume (160 mL), a better Y_w ($\sim$24 %) and process yield ($\sim$79 %) with less solvent discarded (20 %). This shows that even for the best performing LPE dispersion, the HPH counterpart is still better across all of the metrics.

For the exfoliation of In_2Se_3 and Bi_2Te_3, the concentrations obtained *via* HPH are lower than those obtained for the other materials. The concentrations of the LPE dispersions are still matched and the metrics compared. For LPE In_2Se_3 the Y_w is 3.3 %, the process yield is 12.8 %, the percentage solvent discarded is 85.4 % with a total volume of dispersion obtained at 65 mL. The HPH In_2Se_3 dispersion showed consistently better values for these metrics, 7.7 %, 82.5 %, 16.5 % and 167 mL, respectively. This is the highest volume obtained for all of the HPH samples which led to the highest process yield and lowest amount of solvent discarded during any of the dispersion processes in this work. The final material tested in this work is Bi_2Te_3, which showed Y_w of 1.6 %, process yield of 12.3 %, percentage solvent discarded of 86.0 % and a total dispersion volume obtained of 37 mL for the LPE dispersion against 4.28 %, 80.5 %, 18.5 % and 163 mL, respectively, for the HPH dispersion.

All of the data from Figure 3A concur and show that faster, higher yielding and more efficient exfoliation of different layered materials are achieved consistently using HPH over conventional ultrasound-assisted LPE dispersion techniques. The process yield of the LPE dispersions of all the materials exfoliated is $<$20 %, with the highest reported for *h*-BN at 18.3 %. On the other hand, for the HPH dispersions, the process yield is always $>$75 %, with a high of 82.5 % reported for In_2Se_3. This is clear evidence that stabiliser-free HPH exfoliation of 2D-materials is more efficient than the LPE analogue, while consisting of a simpler, faster process with less waste generation. We note that the optimised HPH parameters for MoS_2 are used for all the other materials. Therefore, further improvements could be made in their exfoliation with individual optimisation. A detailed discussion on how HPH parameters can be tailored for different 2D materials is provided in Supplementary Note 2.

We next determine any changes to the material during the exfoliation process by conducting Raman spectroscopy on the powdered crystal, HPH and LPE exfoliated material; Figure 3B. The Raman spectra of the MoS_2 samples show characteristic E^1_{2g} and A_{1g} peaks around 383 cm^{-1} and 408 cm^{-1}, respectively, indicating that the material is not adversely affected by the exfoliation[63]. Note that although we expect a shift in peaks for mono-/bi- layer sheets[63] but as we drop-cast our Raman samples, we are unlikely to single out individual flakes which would

make any such shift more apparent. Complementary structural analysis by X-ray diffraction (Figure S5) further confirms the preservation of the crystalline phase. All diffraction peaks can be indexed to the hexagonal 2H-MoS_2 structure (JCPDS No. 37-1492)[64], and no additional reflections or shoulders are observed, ruling out oxidation (e.g., MoO_3) or phase transformation during high-pressure homogenization. Additionally, HRTEM reveals a distinct 0.27 nm lattice fringe corresponding to the (100) plane of 2H-MoS_2, confirming the preservation of its hexagonal crystal structure after HPH exfoliation (Figure S6). These results collectively indicate that the exfoliation process retains the intrinsic crystal structure of MoS_2.

We see similar results for $MoSe_2$ samples which express E_{1g} and A_{1g} at 168 cm^{-1} and 242 cm^{-1}, respectively[65]. For *h*-BN the characteristic E_{2g} peak at $\sim$ 1366 cm^{-1} is observed for all of the samples[66]. There is a small shift ($\sim$1 cm^{-1}) of the HPH *h*-BN spectrum, which centres at 1367 cm^{-1}, shifting in the direction expected for mono-few layer *h*-BN[67]. However, we note that this shift alone cannot be used to make a clear conclusion of greater exfoliation as it is within the measurement error margin. The spectrum for In_2Se_3 exhibits a high signal to nose ratio for the bulk material, but noisier spectra for the exfoliated samples. However we are still able to identify the characteristic peaks[68,69]: E^2 ($\sim$89 cm^{-1}), A_1^1 ($\sim$104 cm^{-1}), E^4 ($\sim$180 cm^{-1}), A_1^2 ($\sim$182 cm^{-1}) and A_1^3 ($\sim$193 cm^{-1}). Despite the noisier spectra, we conclude from the similarity of the spectra that the material is not adversely affected by the exfoliation process.

Our final Raman spectra set is that of Bi_2Te_3. All of the spectra exhibit characteristic E_g^1 ($\sim$40 cm^{-1}), A_{1g}^1 ($\sim$62 cm^{-1}), E_g^2 ($\sim$101 cm^{-1}) and A_1^2g ($\sim$140 cm^{-1}) modes[70]. However, only the spectra of the exfoliated Bi_2Te_3 contain the A_{1u} ($\sim$118 cm^{-1}) mode. The omission of the A_{1u} from the bulk spectrum is characteristic, and so serves as clear evidence from Raman for the exfoliation of Bi_2Te_3 by both HPH and LPE. We can get some more information from the spectra of the HPH and LPE samples by evaluating the value of $I(A_{1g}^2)/I(E_g^2)$ and $I(A_{1u})/I(E_g^2)$, which have a higher value with thinner material *i.e.* better exfoliation[70]. The $I(A_{1g}^2)/I(E_g^2)$ is 0.95 for HPH and 0.91 for LPE exfoliated Bi_2Te_3, similar for the two methods. The $I(A_{1u})/I(E_g^2)$ gives more insight into the differences in the processes with values of 1.15 for HPH and 0.98 for LPE, indicating that the degree of exfoliation with HPH is marginally better. We again note that the Raman data gives an insight into the exfoliation, but without a definitive conclusion. Therefore, to verify the differences further, we conduct AFM statistical analysis of both HPH and LPE exfoliated samples.

In Figure 3C, we plot the data from our AFM studies as bar charts showing the average and standard deviation of the lateral flake size and height. We observe that the HPH exfoliated material is always statistically smaller and thinner, with smaller variations in both lateral size and height across the measured flakes. This is explained by the material in the HPH samples being subjected to shear forces applied uniformly across the entirety of the mixture repeatedly as opposed to more localised forces in the sonication assisted LPE dispersion. From this comparative study of HPH and LPE exfoliation for a range of 2D-materials, we determine that stabiliser free exfoliation *via* HPH is a faster, less wasteful method to exfoliate 2D-materials that yields material that is more consistent in size/thickness. This translates to a more desirable method for large scale exfoliation for a range of materials, offering scope to exploit their varied properties for target applications. While our HPH exfoliation method is demonstrated at laboratory scale, we emphasize that HPH is inherently a continuous and industrially scalable technique. Commercial HPH systems operating at comparable pressures and capable of handling flow rates exceeding hundreds of liters per hour are already widely adopted in the pharmaceutical and food industries[71,72]. Unlike batch-based exfoliation techniques, the flow-through nature of HPH enables straightforward scale-up by increasing the cycle number or employing higher-capacity chambers. Moreover, the use of low-toxicity solvents (e.g., IPA) and the absence of stabilizers simplifies post-processing and mitigates the environmental impact. We acknowledge that scale-up introduces engineering challenges, such as flow stability, microchannel erosion, and

temperature control. However, these factors are well managed in existing industrial HPH platforms. These issues have been extensively studied and addressed in industrial practice, and we suggest that the associated techniques could be translated to the exfoliation of two-dimensional materials.[71,73] The exfoliation of the material is the first step to implementing it for its intended purpose. The final step of the process is the deposition of the exfoliated material into a device configuration. We select inkjet printing to deposit our exfoliated material, as it allows reliable and repeatable small scale prototyping with binder free ink formulations unlike the majority of the other printing processes[11,74,75]. Indeed, inkjet printing is a non-contact, direct writing technology that has been used extensively in the accurate deposition of 2D materials for a range of electronic and optoelectronic devices and sensors[3,5,6,9,57,76,77]. With the absence of a stabiliser, we use a binary solvent ink formulation, consisting of IPA and 2-butanol in a 9:1 ratio, designed to facilitate uniform inkjet printing avoiding the non-uniform coffee ring depositions[5]. Since the MoS_2 is already dispersed in IPA, our ink formulation requires addition of 2-butanol in the correct ratio and stirring for 5 minutes. Using this step, we formulate ink from the HPH and LPE dispersions to be used as the active material in Ag-MoS_2-Au memristors, to evaluate performance differences of the resultant devices. The differences in exfoliated MoS_2 flakes obtained via HPH and LPE, such as flake size, uniformity, and defect density, directly influence the ink properties and subsequently the printed memristor performance.

Performance of HPH- and LPE-Exfoliated MoS_2 Memristors

As an emerging next-generation memory device, memristors are attracting a lot of interest from researchers. A memristor is a passive circuit element, whose function cannot be replicated by any combination of fundamental circuit elements[78]. They are two-terminal "memory resistors" that retain internal resistance states based on previously applied voltage and current that can behave as a resistive switch[79]. The SET-RESET operation allows individual memristors to switch between low resistance state (LRS) and high resistance state (HRS), enabling the conversion and storage of logic 1's and 0's. As the reverse of the SET process, the RESET operation through the application of a suitable negative voltage returns the device to high resistance state (HRS). Memristor arrays empower in-memory computing[80], avoiding the time delays and energy consumption associated with the repeated movement of data between storage and computing units. They show potential to become a core technology to support emerging AI and IoT applications.

One possible memristor architecture is based on a conductor/insulator/conductor thin film stack, where the insulating switching material is traditionally in the form of a metal oxide. State of the art metal oxide memristor devices exhibit nanosecond programming times, high switching ratio, low energy consumption, high cycling endurance and retention times of several years[81]. Compared to traditional CMOS manufacturing processes, inkjet printing technology offers the potential for low-cost, large-area manufacturing and the ability to deposit materials on conformal and flexible substrates, making it ideal for the smart wearables and robotics. However, flexible and printable metal oxide memristors exhibit poorer characteristics, with high operating voltage ($>$2 V), small dynamic range and low electrical and mechanical reliability[82–85]. As the switching layer, 2D-materials and their composites show great promises, with the potential to exhibit memory features that can outperform conventional bulk material oxides.[86–88]. Specifically, defect-induced conductive pathways in 2D materials can lower the switching voltage and provide more consistent and stable switching pathways, thereby enhancing the overall reliability and endurance of memristor arrays.[37].

The preceding sections establish qualitative differences between the HPH and LPE exfoliated MoS_2 flakes. To identify the process better suited for printed devices, we next fabricate memristors with MoS_2 switching layer on flexible substrates by inkjet printing, which provides a solid

basis for cost-effective fabrication of neuromorphic systems. We start with the Au bottom electrode which is deposited by evaporation on PEL P60 inkjet paper. We next inkjet print the MoS_2 active layer and then the Ag top electrode perpendicular to the Au bottom electrode. Schematic and photograph of an array of 32-memristors are shown in Figure 4A,B, respectively. The inset in Figure 4A shows a micrograph of a single memristor, with a 10-layers of MoS_2 uniformly deposited between the electrodes. We next characterise performance of the memristors made from HPH and LPE exfoliated MoS_2. We aim to demonstrate how the exfoliation method impacts device performance such as switching voltage, ON-OFF ratio, and reliability.

We carry out I-V characterization on 50 memristor devices from each set. The median I-V operation of each memristor (SET) and corresponding statistical distribution are shown in Figure 4C,D respectively for HPH and Figure 4E,F, respectively for LPE MoS_2 based devices. Note that the RESET curves for all of the devices are plotted in Figure S7. From Figure 4C,D, it is apparent that the HPH MoS_2 based memristors possess $>10^3$ ON/OFF ratio at an operation voltage centred at $\sim \pm 1$ V, with $\sim$0.5 V - $\sim$1.5 V range across the 50 memristors. In comparison, although the LPE MoS_2 based memristors show a smaller ON/OFF ratio, they exhibit a greater variability in operation voltage ranging from $\sim$ 0.25 V-$\sim$ 2.25 V (Figure 4E,F) across the 50 devices. The standard deviation of the distributions are calculated, 0.22 for HPH and 0.44 for LPE, underscoring lower performance variability for HPH based memristors. In addition, we evaluate the endurance (Figure S8) and retention (Figure S9) characteristics of the HPH-based devices. The results demonstrate stable resistance states over 100 switching cycles and retention exceeding 5000 seconds, further validating the operational reliability. We attribute this statistically significant difference to the greater uniformity and higher defect density of flakes in the HPH dispersion. Firstly, HPH requires multiple processing cycles, applying high mechanical forces, shear rates, cavitation effects, and frequent collisions and friction, significantly enhancing the exfoliation efficiency of 2D materials[30,39–41]. Simultaneously, these processes introduce structural defects, such as dislocations and vacancies, thereby increasing the defect density. This is supported by Figure S10. The XPS results reveal the stoichiometry of Mo/S with a ratio of 1:1.83, indicating the generation of sulfur defects during the HPH process. We further demonstrate that defect introduction during exfoliation can be modulated by controlling the number of processing cycles (Figure S11). We observe a progressive generation of sulfur vacancies with increasing HPH cycles. These results suggest that HPH provides a promising route for defect engineering of MoS_2 nanoflakes through fine-tuning of processing parameters.

Furthermore, smaller and thinner MoS_2 nanoflakes produced via HPH exhibit a higher sulfur defect density due to the increased edge-to-basal plane ratio[37]. This facilitates the formation of defect-induced conductive pathways and consequently enables lower switching voltages by enhancing the percolation of conductive paths within the memristor. Moreover, the uniformity of the HPH-exfoliated flakes ensures a consistent average sulfur defect percolation length, thereby reducing cycle-to-cycle switching voltage variations and enhancing device reliability. These observations align with insights into defect engineering in memristive systems. A moderate density of atomic defects is generally beneficial for facilitating conductive filament formation, resulting in lower SET voltages and improved energy efficiency[89]. It also contributes to increased conduction channels in the low-resistance state (LRS), lowering effective resistance. However, excessive defect densities can lead to elevated leakage current in the high-resistance state (HRS), narrowing the resistance window and compromising data retention and off-state reliability.[90] Therefore, both the defect density and its spatial distribution must be carefully optimized, as an intermediate density with a uniform distribution can achieve an optimal balance between reliable switching and device endurance.

We also fabricate 50 memristors from our recollected-MoS_2 samples to evaluate any differences in performance from the original HPH and LPE based memristors. The median I-V operation of each recollected MoS_2 memristor (SET) is shown in Figure S12A (RESET curve shown

in Figure S7). These devices have a lower ON/OFF ratio than both HPH and LPE based memristors. We attribute this poor performance to the concentration of the ink, which is considerably lower for the recollected MoS_2, leading to a smaller amount and hence thinner active material layer being deposited between the electrodes. The distribution of the SET voltage (Figure S12B) is considerably narrower than LPE memristors and slightly narrower than HPH memristors, with a standard deviation of 0.20. This again is attributed to a smaller distribution of flake size within the ink (Figure S2C). This data shows that the recollected MoS_2 from the first round of HPH could be recycled and used as a functional material in printed devices.

We note that the optimisation of the device structure/performance fabricated from the HPH and LPE MoS_2 inks is beyond the scope of this work, with the device fabrication conducted with the aim of allowing a fair comparison between the material obtained from both processes. With optimisation of the ink concentration and the number of layers printed, the performance of the MoS_2 memristors can be improved.[91] On the other hand, the printing of HPH exfoliated material serves as proof that HPH can be implemented as a mature, scalable production method to obtain directly exfoliated nanomaterial for functional devices. To further demonstrate the versatility of HPH-exfoliated materials for inkjet-printed memristors, we fabricate 2D heterostructure memristor with an Au/h-BN/MoS_2/Ag architecture (Figure S13). The device exhibits excellent threshold resistive switching characteristics, including a low operating voltage of $\sim$0.2 V and an ON/OFF ratio exceeding 10^4. These results further highlight the potential of using tailored HPH-exfoliated 2D materials to engineer diverse high-performance memristive devices.

In summary, the HPH process demonstrates a simple, fast, high throughput method of exfoliation that utilises relatively benign, commonly used IPA as the solvent. The resulting dispersion is stabiliser-free, with a considerably high concentration of 2D-materials with recoverable stability. The HPH has a process yield of $>$75 % as opposed to $<$20 % for LPE for a range of 2D-materials. Crucially, the HPH process produces a fraction of the waste compared to the LPE process, which uses harsh/toxic solvents to achieve stabiliser-free exfoliation. The use of these solvents complicates the LPE process, with potential scale up impacts on cost, safety and environmental footprint. Furthermore, a Life Cycle Assessment (LCA) analysis reveals that, using MoS_2 as an example, the HPH process achieves a 98.4% reduction in emissions per gram of product compared to LPE. This significant reduction in carbon emissions highlights the potential of HPH in promoting low-carbon manufacturing practices, making it a more sustainable approach for large-scale exfoliation of 2D materials. The uniformity of HPH exfoliated materials over LPE counterparts is also reflected in the narrower statistical performance variation of corresponding inkjet printed memristors. Although there is scope for further process optimisation for HPH, we have set the foundation and shown the viability of this process as a low-waste and stabiliser-free method for large-scale exfoliation of 2D-materials.

METHODS

Material Dispersion

All chemicals and nanomaterial powders are purchased from Sigma Aldrich and used as received. MoS_2, $MoSe_2$, *h*-BN, In_2Se_3 and Bi_2Te_3 are all exfoliated using both LPE and HPH.

Ultrasound assisted liquid phase exfoliation, LPE

10 mg.mL^{-1} of nanomaterial powder and NMP is mixed and added to a glass sonication vial. The solution is sonicated for 12 hours using a Fisher FB15050 ultrasonic bath and then subjected to 1 hour of centrifugation at 1000 rpm for 1 hour. The top 95% of the dispersion is collected and further centrifuged in a Beckman Coulter Proteome XL-A, with a SW32 Ti rotor, at average *g*-value of $\sim$50,000 (20,000 rpm) for 1 hour. The supernatant is discarded and the remaining sediment is collected and redistributed in 60 mL of IPA, completing the solvent exchange. The high speed centrifugation ($\sim$50,000 *g*) and dispersion in fresh IPA is repeated twice more to remove any residual NMP. A final, high-speed centrifugation step to wash the sample for a final time is conducted and the sediment is dispersed in a smaller amount of fresh IPA, yielding the final, concentrated dispersion.

High pressure homogenisation, HPH

A premix is prepared by dispersing the 2D material powder in isopropyl alcohol (IPA) at the desired concentration, with 10 mg mL^{-1} identified as optimal. This premix is then directly fed into the high-pressure homogenizer (HPH) and processed for the desired number of cycles. The homogenization pressure is set to 1500 bar unless otherwise specified, and the selected microchannel diameter is 87 μm. Upon completion of the HPH process, the exfoliated dispersion is collected from the homogenizer outlet and subjected to low-speed centrifugation at 1000 rpm for 1 hour. The resulting supernatant is collected and used as the final exfoliated dispersion.

UV/Vis spectroscopy

All optical absorption measurements of the dispersions are carried out in a Cary 7000 UV–vis-NIR Spectrometer under absorption mode, using a 10 mm quartz cuvette.

Atomic force microscopy

AFM measurements of the exfoliated flakes are taken with a Bruker Dimension Icon in scan assist mode. Samples are diluted at least 100 times and then drop cast on to pre-cleaned (acetone/IPA) Si/SiO_2 substrate. The sample is heated to 80 $^\circ$C.

Raman spectroscopy

Raman measurements are performed using a Horiba LabRAM Evolution Raman spectrometer with 532 nm laser excitation at a laser power of 400 μW. The confocal hole is set at 100 μm. The measurements are obtained with an acquisition time of 15 s and 3 accumulations.

Fabrication of memristors

A stencil mask is used to deposit 5 nm chromium and 20 nm gold on the paper substrate using an E306A thermal evaporator. The paper substrate used is PEL P60 inkjet paper. The substrate is then placed on the platen of the Dimatix Materials Printer at 60℃. The MoS_2 ink is diluted to 2 mg.ml^{-1} and printed with a drop spacing of 25 μm as active layer. The silver top electrode is printed using a silver nanoparticle ink (Sigma) with a drop spacing of 25 μm. The printed silver ink is transformed into conductive electrode by annealing the samples at 100 $^{\circ}$C for 1 hour in a nitrogen glove box.

Electrical characterisation

Room-temperature electrical measurement is conducted in a Suss MicroTec Probe Station connected to semiconductor parameter analyser (Keysight B2902A). During all electrical measurements, the bottom electrode is kept grounded while the top electrode is biased.

XPS

XPS analysis is performed using a Thermo NEXSA G2 XPS equipped with a monochromated Al Kα X-ray source (1486.7 eV), a spherical sector analyzer, and three multichannel resistive plate 128-channel delay line detectors. All data are recorded at 19.2 W with an X-ray beam size of 400 $\times$ 200 μm. Survey scans are acquired at a pass energy of 200 eV, and high-resolution scans at a pass energy of 50 eV. Electronic charge neutralization is achieved using an ion source (Thermo Scientific FG-03) with an ion gun current of 150 μA and an ion gun voltage of 40 V. All measurements are conducted at a pressure below 10^{-8} Torr and a room temperature of 294 K. Sample surface cleaning is carried out using a 2 keV cluster source for 30 seconds. Data are analyzed using CasaXPS v2.3.26rev1.0N. Peaks are fitted with a Shirley background prior to component analysis, and LA(1.53,243) line shapes are employed to fit the components.

RESOURCE AVAILABILITY

Lead contact

Requests for further information and resources should be directed to and will be fulfilled by the lead contact, Tawfique Hasan (th270@cam.ac.uk).

Materials availability

This study does not generate new materials.

Data and code availability

- All data of this study are available within the article and supplemental information.
- This paper does not report original code.
- Any additional information required to reanalyze the data reported in this paper is available from the lead contact upon request.

ACKNOWLEDGMENTS

The authors acknowledge funding support from Engineering and Physical Sciences Research Council (EP/T014601/1, EP/W024284/1), China Scholarship Council, King Abdulaziz City for Science and Technology (KACST) and Marie Vergottis Cambridge Trust. The authors thank all members of the lab for their support.

AUTHOR CONTRIBUTIONS

J.C., N.M., T. B. carried out HPH and LPE experiments. J.C. and A.A. fabricated the memristor devices. J.C., A.A. and G.P. performed device characterization. N.M., B. Z. and M.X. conducted AFM characterization. N.M. and B. Z. conducted Raman spectroscopy measurement. Z. C. conducted FTIR and TEM characterization. S. G. conducted XPS characterization. N.M. and O. O. conducted nanoflake sedimentation test. T.H. directed and coordinated the research. J.C., N. M. and T.H. wrote the manuscript.

DECLARATION OF INTERESTS

The authors declare no competing interests.

SUPPLEMENTAL INFORMATION INDEX

Figures S1-S13 and their legends in a PDF

Table S1-S9 and their titles in a PDF

MAIN FIGURE TITLES AND LEGENDS

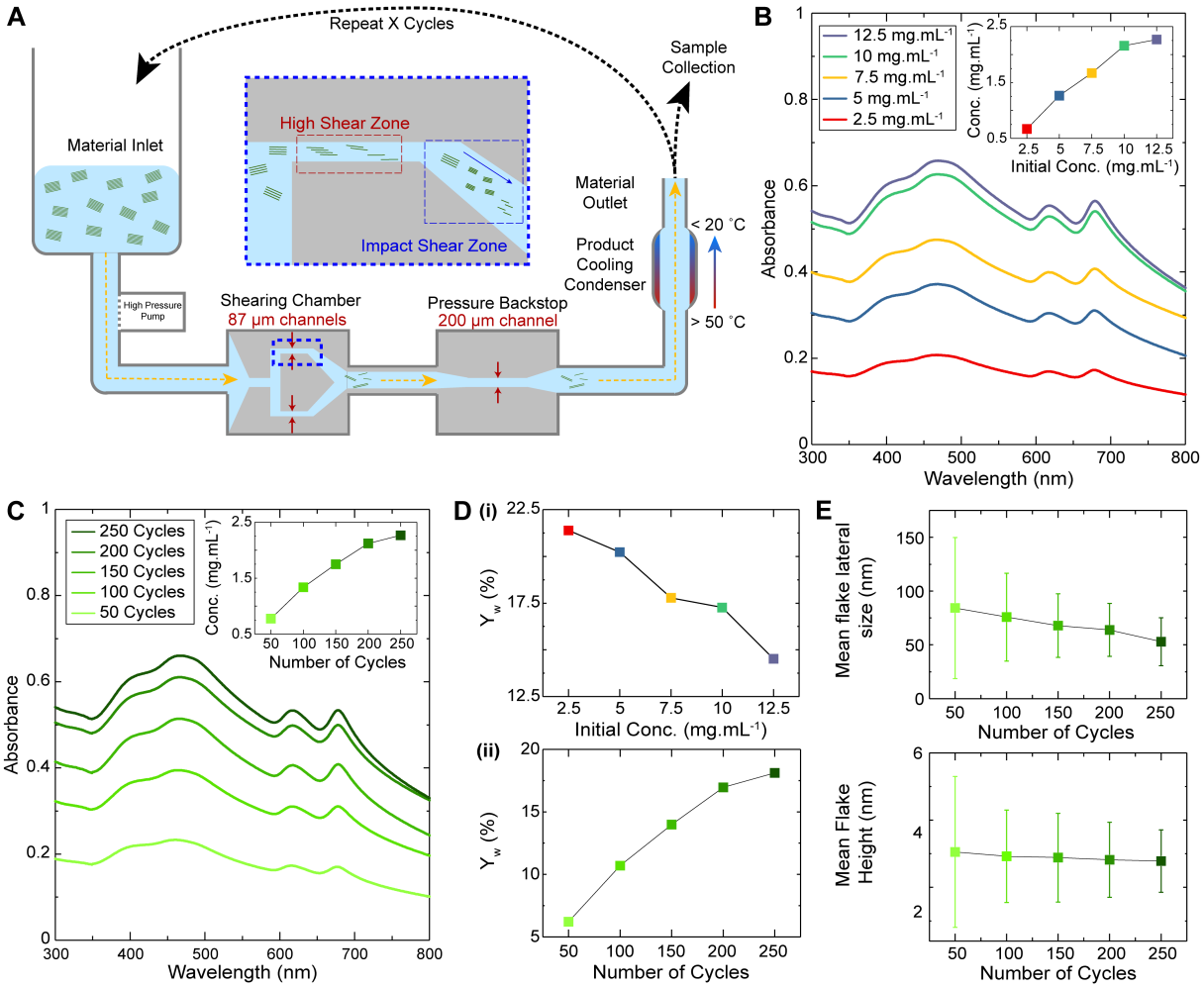

Figure 1. Overview of the HPH system and optimization of exfoliation parameters for MoS_2 dispersions

(A) Schematic of a HPH system, with an inset detailing the inner structure of the micro-channel. (B) UV/Vis spectra of the dispersions obtained during the optimisation of the initial concentration for MoS_2 exfoliation by HPH, inset shows the effect on the final concentration. (C) UV/Vis spectra of the dispersions obtained during the optimisation of the number of cycles for MoS_2 exfoliation by HPH, inset shows the effect on the final concentration. (D) Graphs showing the effect on the yield of MoS_2 dispersed, Y_w, of (i) the initial concentration and (ii) the number of cycles the sample is processed. (E)Graphs presenting the AFM statistics obtained for samples yielded from 50-250 cycles of processing.

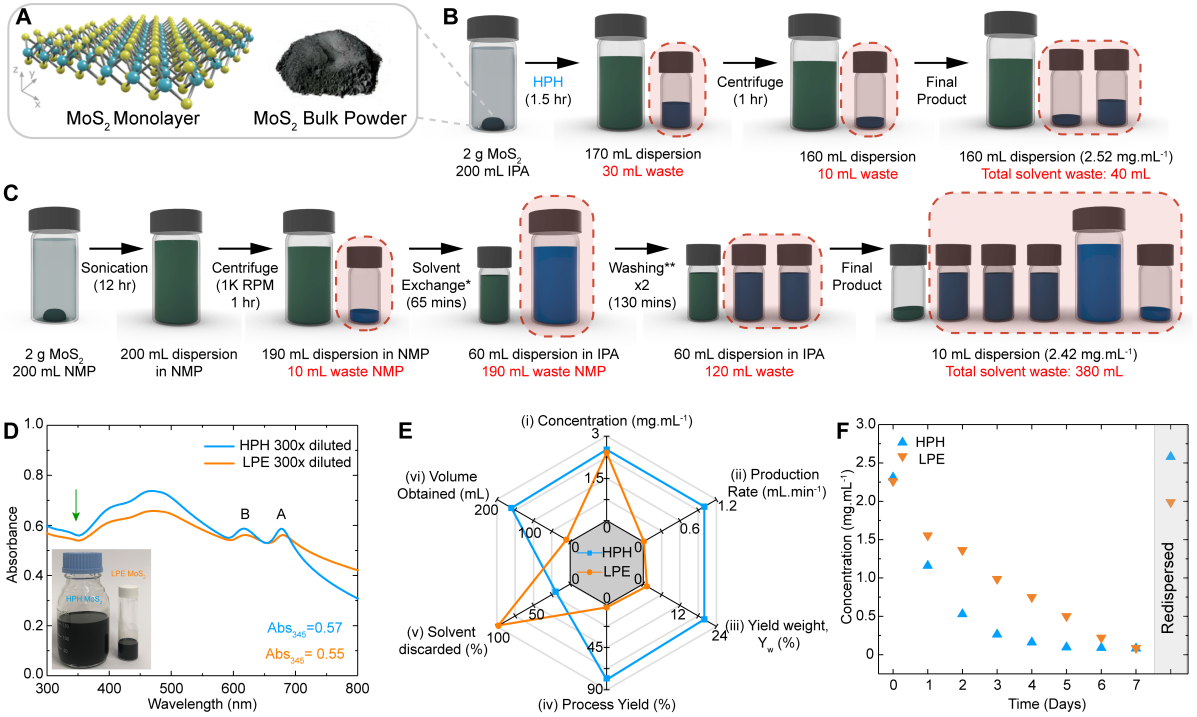

Figure 2. Comparison of HPH and LPE processes for MoS_2 exfoliation

(A) 3D structure of MoS_2 monolayer with a photograph of bulk MoS_2 powder.
(B) Schematic representation of the HPH process, outlining the product and any waste from each step of the process.
(C) Schematic representation of the LPE process, outlining the product and any waste from each step of the LPE process.
(D) UV/Vis of the MoS_2 samples dispersed by HPH and LPE with a photograph of the samples in the inset.
(E) Radar plot comparing key process metrics for HPH and LPE exfoliation of MoS_2.
(F)Scatter plot showing the results of a seven day stability test conducted on HPH and LPE MoS_2 obtained.

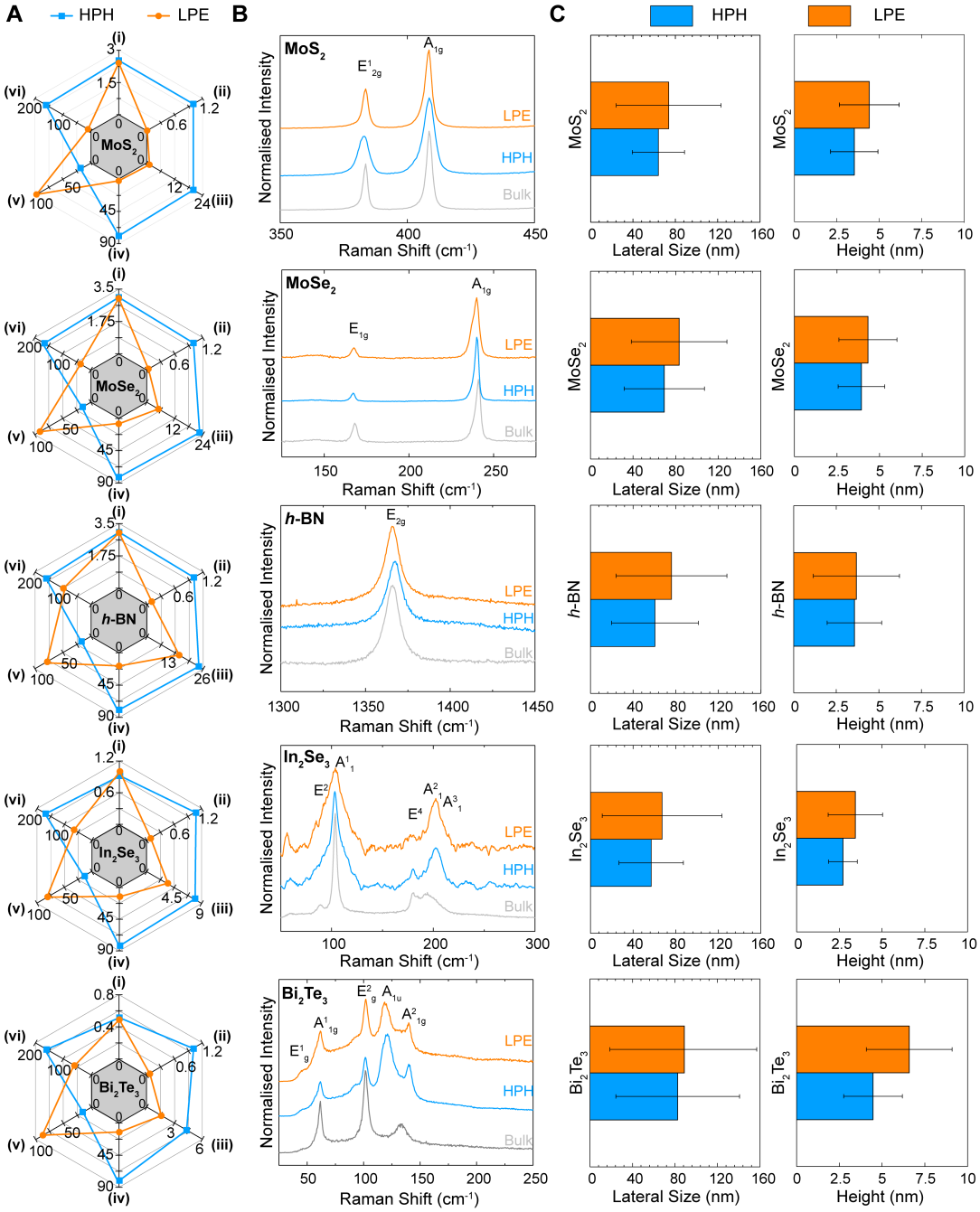

Figure 3. Comparison of HPH and LPE for the exfoliation of different materials. From top to bottom, the materials are MoS_2, $MoSe_2$, *h*-BN, In_2Se_3 and Bi_2Te_3

(A) Radar plots displaying the comparison of HPH and LPE for (i) concentration ($mg.mL^{-1}$) (ii) production rate ($mL.min^{-1}$) (iii) yield weight, Y_w, (%) (iv) process yield (%) (v) solvent discarded (%) and (vi) the volume of dispersion obtained (mL).
(B) Raman spectra of the bulk, HPH exfoliated and LPE exfoliated samples of each material.
(C) Bar graphs depicting the AFM statistics for the HPH and LPE samples, comparing the lateral size and thickness of the flakes yielded from both processes.

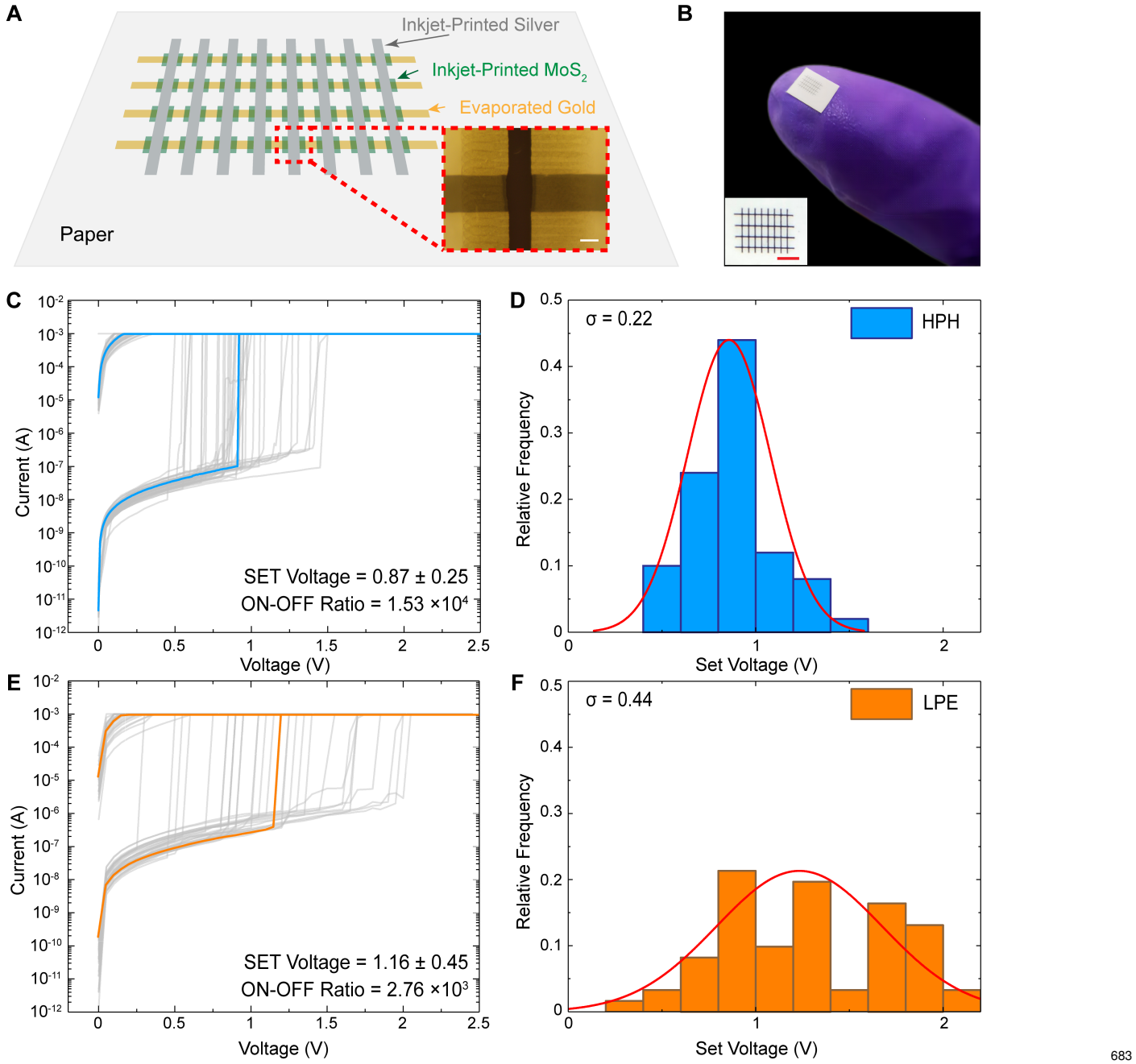

Figure 4. Device performance statistics of inkjet-printed memristors based on HPH- and LPE-exfoliated MoS_2 inks

(A) Schematic of the 32-device array Au-MoS_2-Ag memristor structure used in this work. Inset is an optical microscope image of a single device, scale bar = 100 μm.
(B) Photograph of the 32-device array on a fingertip, the inset is a zoomed photograph of the array on paper (scale bar = 1 mm).
(C) Median I-V operations of 50 memristors fabricated using the HPH MoS_2 ink as the active material. (D) The histogram is the statistical distribution of the set voltage in the the I-V operations for HPH MoS_2 devices.
(E) Median I-V operations of 50 memristors fabricated using the LPE MoS_2 ink as the active material.
(F) Statistical distribution of the set voltage in the I-V operations for LPE MoS_2 devices.

References

1. Novoselov, K.S., Geim, A.K., Morozov, S.V., Jiang, D., Zhang, Y., Dubonos, S.V., Grigorieva, I.V., and Firsov, A.A. (2004). Electric field effect in atomically thin carbon films. Science *306*, 666–669. URL: http://www.ncbi.nlm.nih.gov/pubmed/15499015. doi: 10.1126/science.1102896.

2. Bonaccorso, F., Lombardo, A., Hasan, T., Sun, Z., Colombo, L., and Ferrari, A.C. (2012). Production and processing of graphene and 2d crystals. Materials Today *15*, 564–589. URL: http://dx.doi.org/10.1016/S1369-7021(13)70014-2. doi: 10.1016/S1369-7021(13)70014-2.

3. McManus, D., Vranic, S., Withers, F., Sanchez-Romaguera, V., Macucci, M., Yang, H., Sorrentino, R., Parvez, K., Son, S.K., Iannaccone, G., Kostarelos, K., Fiori, G., and Casiraghi, C. (2017). Water-based and biocompatible 2D crystal inks for all-inkjet-printed heterostructures. Nature Nanotechnology *12*, 343–350. URL: www.nature.com/naturenanotechnology. doi: 10.1038/nnano.2016.281.

4. Worsley, R., Pimpolari, L., McManus, D., Ge, N., Ionescu, R., Wittkopf, J.A., Alieva, A., Basso, G., MacUcci, M., Iannaccone, G., Novoselov, K.S., Holder, H., Fiori, G., and Casiraghi, C. (2019). All-2D Material Inkjet-Printed Capacitors: Toward Fully Printed Integrated Circuits. ACS Nano *13*, 54–60. URL: www.acsnano.org. doi: 10.1021/acsnano.8b06464.

5. Hu, G., Yang, L., Yang, Z., Wang, Y., Jin, X., Dai, J., Wu, Q., Liu, S., Zhu, X., Wang, X., Wu, T.C., Howe, R.C.T., Albrow-Owen, T., Ng, L.W.T., Yang, Q., Occhipinti, L.G., Woodward, R.I., Kelleher, E.J., Sun, Z., Huang, X., Zhang, M., Bain, C.D., and Hasan, T. (2020). A general ink formulation of 2D crystals for wafer-scale inkjet printing. Science Advances *6*, 5029–5041. URL: http://advances.sciencemag.org/. doi: 10.1126/sciadv.aba5029.

6. Hu, G., Albrow-Owen, T., Jin, X., Ali, A., Hu, Y., Howe, R.C., Shehzad, K., Yang, Z., Zhu, X., Woodward, R.I., Wu, T.C., Jussila, H., Wu, J.B., Peng, P., Tan, P.H., Sun, Z., Kelleher, E.J., Zhang, M., Xu, Y., and Hasan, T. (2017). Black phosphorus ink formulation for inkjet printing of optoelectronics and photonics. Nature Communications *8*. URL: https://www.nature.com/articles/s41467-017-00358-1.pdf. doi: 10.1038/s41467-017-00358-1.

7. Francis, B.M., Ponraj, J.S., Dhanabalan, B., Manavalan, R.K., Veluswamy, P., Yin, P., Al-Hartomy, O.A., Al-Ghamdi, A., Wageh, S., Zhang, H., and Dhanabalan, S.C. (2022). Two-dimensional material-based printed photonics: A review. 2D Materials *9*. doi: 10.1088/2053-1583/ac5411.

8. Dai, J., Ogbeide, O., Macadam, N., Sun, Q., Yu, W., Li, Y., Su, B.L., Hasan, T., Huang, X., and Huang, W. (2020). Printed gas sensors. Chemical Society Reviews *49*, 1756–1789. doi: 10.1039/c9cs00459a.

9. Ogbeide, O., Bae, G., Yu, W., Morrin, E., Song, Y., Song, W., Li, Y., Su, B., An, K., and Hasan, T. (2022). Inkjet-Printed rGO/binary Metal Oxide Sensor for Predictive Gas Sensing in a Mixed Environment. Advanced Functional Materials pp. 2113348. doi: 10.1002/adfm.202113348.

10. Bonaccorso, F., Bartolotta, A., Coleman, J.N., and Backes, C. (2016). 2D-Crystal-Based Functional Inks. Advanced Materials *28*, 6136–6166. doi: 10.1002/adma.201506410.

11. Hu, G., Kang, J., Ng, L.W., Zhu, X., Howe, R.C., Jones, C.G., Hersam, M.C., and Hasan, T. (2018). Functional inks and printing of two-dimensional materials. Chemical Society Reviews *47*, 3265–3300. URL: https://pubs.rsc.org/en/content/articlepdf/2018/cs/c8cs00084k. doi: 10.1039/c8cs00084k.

12. Hummers, W.S., and Offeman, R.E. (1958). Preparation of Graphitic Oxide. Journal of the American Chemical Society *80*, 1339. URL: https://pubs.acs.org/sharingguidelines. doi: 10.1021/ja01539a017.

13. Coleman, J.N., Lotya, M., O'Neill, A., Bergin, S.D., King, P.J., Khan, U., Young, K., Gaucher, A., De, S., Smith, R.J., Shvets, I.V., Arora, S.K., Stanton, G., Kim, H.Y., Lee, K., Kim, G.T., Duesberg, G.S., Hallam, T., Boland, J.J., Wang, J.J., Donegan, J.F., Grunlan, J.C., Moriarty, G., Shmeliov, A., Nicholls, R.J., Perkins, J.M., Grieveson, E.M., Theuwissen, K., McComb, D.W., Nellist, P.D., and Nicolosi, V. (2011). Two-dimensional nanosheets produced by liquid exfoliation of layered materials. Science *331*, 568–571. URL: http://science.sciencemag.org/. doi: 10.1126/science.1194975.

14. Eda, G., Yamaguchi, H., Voiry, D., Fujita, T., Chen, M., and Chhowalla, M. (2011). Photoluminescence from chemically exfoliated MoS_2. Nano Letters *11*, 5111–5116. URL: https://pubs.acs.org/sharingguidelines. doi: 10.1021/nl201874w.

15. Yao, Y., Lin, Z., Li, Z., Song, X., Moon, K.S., and Wong, C.P. (2012). Large-scale production of two-dimensional nanosheets. Journal of Materials Chemistry *22*, 13494–13499. doi: 10.1039/c2jm30587a.

16. Biccai, S., Barwich, S., Boland, D., Harvey, A., Hanlon, D., McEvoy, N., and Coleman, J.N. (2019). Exfoliation of 2D materials by high shear mixing. 2D Materials *6*. doi: 10.1088/2053-1583/aae7e3.

17. Yang, S., Zhang, P., Nia, A.S., and Feng, X. (2020). Emerging 2D Materials Produced via Electrochemistry. Advanced Materials *32*. doi: 10.1002/adma.201907857.

18. Hernandez, Y., Nicolosi, V., Lotya, M., Blighe, F.M., Sun, Z., De, S., McGovern, I.T., Holland, B., Byrne, M., Gun'ko, Y.K., Boland, J.J., Niraj, P., Duesberg, G., Krishnamurthy, S., Goodhue, R., Hutchison, J., Scardaci, V., Ferrari, A.C., and Coleman, J.N. (2008). High-yield production of graphene by liquid-phase exfoliation of graphite. Nature Nanotechnology *3*, 563–568. URL: www.nature.com/naturenanotechnology. doi: 10.1038/nnano.2008.215.

19. Lotya, M., Hernandez, Y., King, P.J., Smith, R.J., Nicolosi, V., Karlsson, L.S., Blighe, F.M., De, S., Wang, Z., Mcgovern, I.T., Duesberg, G.S., and Coleman, J.N. (2009). Liquid Phase Production of Graphene by Exfoliation of Graphite in Surfactant/Water Solutions. Journal of the American Chemical Society *131*, 3611–3620. URL: http://pubs.acs.org/doi/pdf/10.1021/ja807449u. doi: 10.1021/ja807449u.

20. Hu, C.X., Shin, Y., Read, O., and Casiraghi, C. (2021). Dispersant-assisted liquid-phase exfoliation of 2D materials beyond graphene. Nanoscale *13*, 460–484. doi: 10.1039/d0nr05514j.

21. Ravichandran, V., and Varrla, E. (2025). Sustainable high-yield h-BN nanosheet production by liquid exfoliation for thermal interface materials. RSC Applied Interfaces *2*, 534–549. doi: 10.1039/d4lf00338a.

22. Guan, G., Zhang, S., Liu, S., Cai, Y., Low, M., Teng, C.P., Phang, I.Y., Cheng, Y., Duei, K.L., Srinivasan, B.M., Zheng, Y., Zhang, Y.W., and Han, M.Y. (2015). Protein induces layer-by-layer exfoliation of transition metal dichalcogenides. Journal of the American Chemical Society *137*, 6152–6155. doi: 10.1021/jacs.5b02780.

23. Shin, Y., Just-Baringo, X., Boyes, M., Panigrahi, A., Zarattini, M., Chen, Y., Liu, X., Morris, G., Prestat, E., Kostarelos, K., Vranic, S., Larrosa, I., and Casiraghi, C. (2021). Enhanced liquid phase exfoliation of graphene in water using an insoluble bis-pyrene stabiliser. Faraday Discussions *227*, 46–60. doi: 10.1039/c9fd00114j.

24. Lin, Z., Liu, Y., Halim, U., Ding, M., Liu, Y., Wang, Y., Jia, C., Chen, P., Duan, X., Wang, C., Song, F., Li, M., Wan, C., Huang, Y., and Duan, X. (2018). Solution-processable 2D semiconductors for high-performance large-area electronics. Nature *562*, 254–258. URL: https://doi.org/10.1038/s41586-018-0574-4http://www.nature.com/articles/s41586-018-0574-4. doi: 10.1038/s41586-018-0574-4.

25. Cunningham, G., Lotya, M., Cucinotta, C.S., Sanvito, S., Bergin, S.D., Menzel, R., Shaffer, M.S., and Coleman, J.N. (2012). Solvent exfoliation of transition metal dichalcogenides: Dispersibility of exfoliated nanosheets varies only weakly between compounds. ACS Nano *6*, 3468–3480. doi: 10.1021/nn300503e.

26. Capelo-Martínez, J.L. (2009). Ultrasound in chemistry: analytical applications. Weinheim: John Wiley & Sons. ISBN 3527319344.

27. Nascentes, C.C., Korn, M., Sousa, C.S., and Arruda, M.A.Z. (2001). Use of Ultrasonic Baths for Analytical Applications: A New Approach for Optimisation Conditions. J. Braz. Chem. Soc *12*, 57–63. doi: 10.1590/S0103-50532001000100008.

28. Chivate, M., and Pandit, A. (1995). Quantification of cavitation intensity in fluid bulk. Ultrasonics Sonochemistry *2*, S19–S25. URL: https://linkinghub.elsevier.com/retrieve/pii/135041779400007F. doi: 10.1016/1350-4177(94)00007-F.

29. Atiemo-Obeng, V.A., and Calabrese, R.V. (2004). Rotor–Stator Mixing Devices. New York, NY: John Wiley & Sons. URL: https://onlinelibrary.wiley.com/doi/full/10.1002/0471451452.ch8https://onlinelibrary.wiley.com/doi/abs/10.1002/0471451452.ch8https://onlinelibrary.wiley.com/doi/10.1002/0471451452.ch8. doi: 10.1002/0471451452.ch8.

30. Paton, K.R., Varrla, E., Backes, C., Smith, R.J., Khan, U., O'Neill, A., Boland, C., Lotya, M., Istrate, O.M., King, P., Higgins, T., Barwich, S., May, P., Puczkarski, P., Ahmed, I., Moebius, M., Pettersson, H., Long, E., Coelho, J., O'Brien, S.E., McGuire, E.K., Sanchez, B.M., Duesberg, G.S., McEvoy, N., Pennycook, T.J., Downing, C., Crossley, A., Nicolosi, V., and Coleman, J.N. (2014). Scalable production of large quantities of defect-free few-layer graphene by shear exfoliation in liquids. Nature Materials 2014 13:6 *13*, 624–630. URL: https://www.nature.com/articles/nmat3944. doi: 10.1038/nmat3944.

31. Carey, T., Alhourani, A., Tian, R., Seyedin, S., Arbab, A., Maughan, J., Šiller, L., Horvath, D., Kelly, A., Kaur, H., Caffrey, E., Kim, J.M., Hagland, H.R., and Coleman, J.N. (2022). Cyclic production of biocompatible few-layer graphene ink with in-line shear-mixing for inkjet-printed electrodes and Li-ion energy storage. npj 2D Materials and Applications *6*. doi: 10.1038/s41699-021-00279-0.

32. Panagiotou, T., Bernard, J.M., and Mesite, S.V. (2008). Deagglomeration and dispersion of carbon nanotubes using microfluidizer® high shear fluid processors. In Technical Proceedings of the 2008 NSTI Nanotechnology Conference and Trade Show, NSTI-Nanotech, Nanotechnology 2008 vol. 1. ISBN 9781420085075 pp. 39–42. URL: www.nsti.org,.

33. Karagiannidis, P.G., Hodge, S.A., Lombardi, L., Tomarchio, F., Decorde, N., Milana, S., Goykhman, I., Su, Y., Mesite, S.V., Johnstone, D.N., Leary, R.K., Midgley, P.A., Pugno, N.M., Torrisi, F., and Ferrari, A.C. (2017). Microfluidization of Graphite and Formulation of Graphene-Based Conductive Inks. ACS Nano *11*, 2742–2755. URL: www.acsnano.org. doi: 10.1021/acsnano.6b07735.

34. Paton, K.R., Anderson, J., Pollard, A.J., and Sainsbury, T. (2017). Production of few-layer graphene by microfluidization. Materials Research Express *4*. doi: 10.1088/2053-1591/aa5b24.

35. He, Y., Andrade, A.F., Ménard-Moyon, C., and Bianco, A. (2024). Biocompatible 2D Materials via Liquid Phase Exfoliation. Advanced Materials *36*, 2310999. doi: 10.1002/adma.202310999.

36. Yang, J.J., Strukov, D.B., and Stewart, D.R. (2013). Memristive devices for computing. Nature Nanotechnology *8*, 13–24. doi: 10.1038/nnano.2012.240.

37. Tang, B., Veluri, H., Li, Y., Yu, Z.G., Waqar, M., Leong, J.F., Sivan, M., Zamburg, E., Zhang, Y.W., Wang, J., and Thean, A.V.Y. (2022). Wafer-scale solution-processed 2D material analog resistive memory array for memory-based computing. Nature Communications *13*, 3037. doi: 10.1038/s41467-022-30519-w.

38. Shi, Y., Liang, X., Yuan, B., Chen, V., Li, H., Hui, F., Yu, Z., Yuan, F., Pop, E., Wong, H.S.P., and Lanza, M. (2018). Electronic synapses made of layered two-dimensional materials. Nature Electronics *1*, 458–465. doi: 10.1038/s41928-018-0118-9.

39. Yi, M., Shen, Z., and Zhu, J. (2014). A fluid dynamics route for producing graphene and its analogues. Chinese Science Bulletin *59*, 1794–1799. doi: 10.1007/s11434-014-0303-9.

40. Yi, M., Shen, Z., Zhang, W., Zhu, J., Liu, L., Liang, S., Zhang, X., and Ma, S. (2013). Hydrodynamics-assisted scalable production of boron nitride nanosheets and their application in improving oxygen-atom erosion resistance of polymeric composites. Nanoscale *5*, 10660–10667. doi: 10.1039/C3NR03714B.

41. Shen, Z., Li, J., Yi, M., Zhang, X., and Ma, S. (2011). Preparation of graphene by jet cavitation. Nanotechnology *22*, 365306. doi: 10.1088/0957-4484/22/36/365306.

42. Feng, X., Li, Y., Wang, L., Chen, S., Yu, Z.G., Tan, W.C., Macadam, N., Hu, G., Huang, L., Chen, L., Gong, X., Chi, D., Hasan, T., Thean, A.V.Y., Zhang, Y.W., and Ang, K.W. (2019). A Fully Printed Flexible MoS_2 Memristive Artificial Synapse with Femtojoule Switching Energy. Advanced Electronic Materials *5*, 1–9. doi: 10.1002/aelm.201900740.

43. Kuo, L., Sangwan, V.K., Rangnekar, S.V., Chu, T.C., Lam, D., Zhu, Z., Richter, L.J., Li, R., Szydłowska, B.M., Downing, J.R., Luijten, B.J., Lauhon, L.J., and Hersam, M.C. (2022). All-Printed Ultrahigh-Responsivity MoS_2 Nanosheet Photodetectors Enabled by Megasonic Exfoliation. Advanced Materials *34*, 2203772. URL: https://doi.org/10.1002/adma.202203772. doi: https://doi.org/10.1002/adma.202203772.

44. Park, K., Woo, K., Kim, J., Lee, D., Ahn, Y., Song, D., Kim, H., Oh, D., Kwon, S., and Lee, Y. (2019). High-Resolution and Large-Area Patterning of Highly Conductive Silver Nanowire Electrodes by Reverse Offset Printing and Intense Pulsed Light Irradiation. ACS Applied Materials & Interfaces *11*, 14882–14891. URL: https://doi.org/10.1021/acsami.9b00838. doi: 10.1021/acsami.9b00838.

45. Finn, D.J., Lotya, M., and Coleman, J.N. (2015). Inkjet Printing of Silver Nanowire Networks. ACS Applied Materials & Interfaces *7*, 9254–9261. URL: https://doi.org/10.1021/acsami.5b01875. doi: 10.1021/acsami.5b01875.

46. Nalawade, Y., Pepper, J., Harvey, A., Griffin, A., Caffrey, D., Kelly, A.G., and Coleman, J.N. (2020). All-Printed Dielectric Capacitors from High-Permittivity, Liquid-Exfoliated BiOCl Nanosheets. ACS Applied Electronic Materials *2*, 3233–3241. URL: https://doi.org/10.1021/acsaelm.0c00561. doi: 10.1021/acsaelm.0c00561.

47. Lu, S., Cardenas, J.A., Worsley, R., Williams, N.X., Andrews, J.B., Casiraghi, C., and Franklin, A.D. (2019). Flexible, Print-in-Place 1D–2D Thin-Film Transistors Using Aerosol Jet Printing. ACS Nano *13*, 11263–11272. URL: https://doi.org/10.1021/acsnano.9b04337. doi: 10.1021/acsnano.9b04337.

48. He, P., Cao, J., Ding, H., Zhao, X., and Li, Z. (2020). Electronic devices based on solution-processed two-dimensional materials. In Synthesis, Modeling, and Characterization of 2D Materials, and Their Heterostructures pp. 351–384.. Elsevier pp. 351–384.

49. Santra, S., Hu, G., Howe, R.C.T., De Luca, A., Ali, S.Z., Udrea, F., Gardner, J.W., Ray, S.K., Guha, P.K., and Hasan, T. (2015). CMOS integration of inkjet-printed graphene for humidity sensing. Scientific Reports *5*, 17374. URL: https://doi.org/10.1038/srep17374. doi: 10.1038/srep17374.

50. Jiang, X., Li, W., Hai, T., Yue, R., Chen, Z., Lao, C., Ge, Y., Xie, G., Wen, Q., and Zhang, H. (2019). Inkjet-printed MXene micro-scale devices for integrated broadband ultrafast photonics. npj 2D Materials and Applications *3*, 34. URL: https://doi.org/10.1038/s41699-019-0117-3. doi: 10.1038/s41699-019-0117-3.

51. Yao, Y., Xia, X., Cheng, Z., Wei, K., Jiang, X., Dong, J., and Zhang, H. (2020). All-Optical Modulator Using MXene Inkjet-Printed Microring Resonator. IEEE Journal of Selected Topics in Quantum Electronics *26*, 1–6. doi: 10.1109/JSTQE.2020.2982985.

52. Varrla, E., Backes, C., Paton, K.R., Harvey, A., Gholamvand, Z., McCauley, J., and Coleman, J.N. (2015). Large-scale production of size-controlled MoS_2 nanosheets by shear exfoliation. Chemistry of Materials *27*, 1129–1139. URL: https://pubs.acs.org/sharingguidelines. doi: 10.1021/cm5044864.

53. Backes, C., Smith, R.J., McEvoy, N., Berner, N.C., McCloskey, D., Nerl, H.C., O'Neill, A., King, P.J., Higgins, T., Hanlon, D., Scheuschner, N., Maultzsch, J., Houben, L., Duesberg, G.S., Donegan, J.F., Nicolosi, V., and Coleman, J.N. (2014). Edge and confinement effects allow in situ measurement of size and thickness of liquid-exfoliated nanosheets. Nature Communications *5*. URL: www.nature.com/naturecommunications. doi: 10.1038/ncomms5576.

54. Alzakia, F.I., Jonhson, W., Ding, J., and Tan, S.C. (2020). Ultrafast Exfoliation of 2D Materials by Solvent Activation and One-Step Fabrication of All-2D-Material Photodetectors by Electrohydrodynamic Printing. ACS Applied Materials and Interfaces *12*, 28840–28851. doi: 10.1021/acsami.0c06279.

55. Zhang, X., Coleman, A.C., Katsonis, N., Browne, W.R., Van Wees, B.J., and Feringa, B.L. (2010). Dispersion of graphene in ethanol using a simple solvent exchange method. Chemical Communications *46*, 7539–7541. URL: www.rsc.org/chemcomm. doi: 10.1039/c0cc02688c.

56. Li, J., Lemme, M.C., and Östling, M. (2014). Inkjet Printing of 2D Layered Materials. ChemPhysChem *15*, 3427–3434. URL: https://doi.org/10.1002/cphc.201402103. doi: https://doi.org/10.1002/cphc.201402103.

57. Carey, T., Cacovich, S., Divitini, G., Ren, J., Mansouri, A., Kim, J.M., Wang, C., Ducati, C., Sordan, R., and Torrisi, F. (2017). Fully inkjet-printed two-dimensional material field-effect heterojunctions for wearable and textile electronics. Nature Communications *8*. URL: www.nature.com/naturecommunications. doi: 10.1038/s41467-017-01210-2.

58. NIST Mass Spectrometry Data Center, William E. Wallace, director (2024). Infrared Spectra in NIST Chemistry WebBook. NIST Standard Reference Database Number 69, Eds. P.J. Linstrom and W.G. Mallard, National Institute of Standards and Technology, Gaithersburg MD, 20899. . https://webbook.nist.gov/chemistry/.

59. ISO 14040:2006 Environmental Management—Life Cycle Assessment—Principles and Framework. International Organization for Standardization (2006). ISO Standard.

60. ISO 14044:2006 Environmental Management—Life Cycle Assessment—Requirements and Guidelines. International Organization for Standardization (2006). ISO Standard.

61. Smoluchowski, M.V. (1916). Drei Vorträge über Diffusion, Brownsche Bewegung und Koagulation von Kolloidteilchen. Physik. Zeit. *17*, 557–585.

62. Verwey, E.J.W., and Overbeek, J.T.G. (1948). Theory of the Stability of Lyophobic Colloids. Amsterdam: North-Holland Publishing Company.

63. Li, H., Zhang, Q., Yap, C.C.R., Tay, B.K., Edwin, T.H.T., Olivier, A., and Baillargeat, D. (2012). From bulk to monolayer MoS_2: Evolution of Raman scattering. Advanced Functional Materials *22*, 1385–1390. doi: 10.1002/adfm.201102111.

64. Joint Committee on Powder Diffraction Standards (2001). Jcpds card no. 37-1492. . International Centre for Diffraction Data (ICDD).

65. Nam, D., Lee, J.U., and Cheong, H. (2015). Excitation energy dependent Raman spectrum of $MoSe_2$. Scientific Reports *5*, 17113. URL: www.nature.com/scientificreports. doi: 10.1038/srep17113.

66. Reich, S., Ferrari, A.C., Arenal, R., Loiseau, A., Bello, I., and Robertson, J. (2005). Resonant Raman scattering in cubic and hexagonal boron nitride. Physical Review B - Condensed Matter and Materials Physics *71*, 1–12. doi: 10.1103/PhysRevB.71.205201.

67. Gorbachev, R.V., Riaz, I., Nair, R.R., Jalil, R., Britnell, L., Belle, B.D., Hill, E.W., Novoselov, K.S., Watanabe, K., Taniguchi, T., Geim, A.K., and Blake, P. (2011). Hunting for monolayer boron nitride: Optical and raman signatures. Small *7*, 465–468. doi: 10.1002/smll.201001628.

68. Lewandowska, R., Bacewicz, R., Filipowicz, J., and Paszkowicz, W. (2001). Raman scattering in α-In_2Se_3 crystals. Materials Research Bulletin *36*, 2577–2583. doi: 10.1016/S0025-5408(01)00746-2.

69. Vilaplana, R., Parra, S.G., Jorge-Montero, A., Rodríguez-Hernández, P., Munoz, A., Errandonea, D., Segura, A., and Manjón, F.J. (2018). Experimental and Theoretical Studies on α-In_2Se_3 at High Pressure. Inorganic Chemistry *57*, 8241–8252. URL: https://pubs.acs.org/sharingguidelines. doi: 10.1021/acs.inorgchem.8b00778.

70. Shahil, K.M., Hossain, M.Z., Teweldebrhan, D., and Balandin, A.A. (2010). Crystal symmetry breaking in few-quintuple Bi_2Te_3 films: Applications in nanometrology of topological insulators. Applied Physics Letters *96*, 153103. URL: https://doi.org/10.1063/1.3396190. doi: 10.1063/1.3396190.

71. GEA Group (2023). Industrial Homogenizers – Ariete Series Brochure. https://www.gea.com/en/products/homogenizers/industrial-homogenizers/. . Accessed: 18 May 2025.

72. Drawell Analytical (2024). The Role of High Pressure Homogenizers in Pharmaceuticals. Drawell Analytical. URL: https://www.drawellanalytical.com/the-role-of-high-pressure-homogenizers-in-pharmaceuticals/. Accessed: 2025-05-17.

73. Microfluidics International Corporation (2024). Microfluidizer® Technology: Consistent Processing and Thermal Control. https://www.microfluidics-mpt.com/microfluidics-technology-and-equipment. . Accessed: 18 May 2025.

74. Macadam, N., Ng, L.W., Hu, G., Shi, H.T.H., Wang, W., Zhu, X., Ogbeide, O., Liu, S., Yang, Z., Howe, R.C., Jones, C., Huang, Y.Y.S., and Hasan, T. (2022). 100 $m.min^{-1}$ Industrial-Scale Flexographic Printing of Graphene-Incorporated Conductive Ink. Advanced Engineering Materials *24*. doi: 10.1002/adem.202101217.

75. Ng, L.W.T., Zhu, X., Hu, G., Macadam, N., Um, D., Wu, T.C., Le Moal, F., Jones, C., and Hasan, T. (2019). Conformal Printing of Graphene for Single- and Multilayered Devices onto Arbitrarily Shaped 3D Surfaces. Advanced Functional Materials pp. 1807933. URL: https://onlinelibrary.wiley.com/doi/abs/10.1002/adfm.201807933. doi: 10.1002/adfm.201807933.

76. Torrisi, F., Hasan, T., Wu, W., Sun, Z., Lombardo, A., Kulmala, T.S., Hsieh, G.W., Jung, S., Bonaccorso, F., Paul, P.J., Chu, D., and Ferrari, A.C. (2012). Inkjet-Printed Graphene Electronics. ACS Nano *6*, 2992–3006. URL: www.acsnano.org. doi: 10.1021/nn2044609.

77. Wu, T.C., De Luca, A., Zhong, Q., Zhu, X., Ogbeide, O., Um, D.S., Hu, G., Albrow-Owen, T., Udrea, F., and Hasan, T. (2019). Inkjet-printed CMOS-integrated graphene–metal oxide sensors for breath analysis. npj 2D Materials and Applications *3*. doi: 10.1038/s41699-019-0125-3.

78. Chua, L.O., and Kang, S.M. (1976). Memristive devices and systems. Proceedings of the IEEE *64*, 209–223. doi: 10.1109/PROC.1976.10092.

79. Yang, J.J., Strukov, D.B., and Stewart, D.R. (2013). Memristive devices for computing. Nature Nanotechnology *8*, 13–24. doi: 10.1038/nnano.2012.240.

80. Yao, P., Wu, H., Gao, B., Tang, J., Zhang, Q., Zhang, W., Yang, J.J., and Qian, H. (2020). Fully hardware-implemented memristor convolutional neural network. Nature *577*, 641–646. URL: http://dx.doi.org/10.1038/s41586-020-1942-4. doi: 10.1038/s41586-020-1942-4.

81. Bessonov, A.A., Kirikova, M.N., Petukhov, D.I., Allen, M., Ryhänen, T., and Bailey, M.J. (2015). Layered memristive and memcapacitive switches for printable electronics. Nature Materials *14*, 199–204. doi: 10.1038/nmat4135.

82. Son, D., Lee, J., Qiao, S., Ghaffari, R., Kim, J., Lee, J.E., Song, C., Kim, S.J., Lee, D.J., Jun, S.W., Yang, S., Park, M., Shin, J., Do, K., Lee, M., Kang, K., Hwang, C.S., Lu, N., Hyeon, T., and Kim, D.H. (2014). Multifunctional wearable devices for diagnosis and therapy of movement disorders. Nature Nanotechnology *9*, 397–404. URL: https://doi.org/10.1038/nnano.2014.38. doi: 10.1038/nnano.2014.38.

83. Kim, S., Jeong, H.Y., Kim, S.K., Choi, S.Y., and Lee, K.J. (2011). Flexible Memristive Memory Array on Plastic Substrates. Nano Letters *11*, 5438–5442. URL: https://doi.org/10.1021/nl203206h. doi: 10.1021/nl203206h.

84. Jang, J., Pan, F., Braam, K., and Subramanian, V. (2012). Resistance Switching Characteristics of Solid Electrolyte Chalcogenide Ag_2Se Nanoparticles for Flexible Nonvolatile Memory Applications. Advanced Materials *24*, 3573–3576. URL: https://doi.org/10.1002/adma.201200671. doi: https://doi.org/10.1002/adma.201200671.

85. Lien, D.H., Kao, Z.K., Huang, T.H., Liao, Y.C., Lee, S.C., and He, J.H. (2014). All-Printed Paper Memory. ACS Nano *8*, 7613–7619. URL: https://doi.org/10.1021/nn501231z. doi: 10.1021/nn501231z.

86. Wang, M., Cai, S., Pan, C., Wang, C., Lian, X., Zhuo, Y., Xu, K., Cao, T., Pan, X., Wang, B., Liang, S.J., Yang, J.J., Wang, P., and Miao, F. (2018). Robust memristors based on layered two-dimensional materials. Nature Electronics *1*, 130–136. URL: https://doi.org/10.1038/s41928-018-0021-4. doi: 10.1038/s41928-018-0021-4.

87. Mazumder, A., Ahmed, T., Mayes, E., Tawfik, S.A., Russo, S.P., Low, M.X., Ranjan, A., Balendhran, S., and Walia, S. (2022). Nonvolatile Resistive Switching in Layered InSe via Electrochemical Cation Diffusion. Advanced Electronic Materials *8*, 2100999. URL: https://doi.org/10.1002/aelm.202100999. doi: https://doi.org/10.1002/aelm.202100999.

88. Chen, S., Mahmoodi, M.R., Shi, Y., Mahata, C., Yuan, B., Liang, X., Wen, C., Hui, F., Akinwande, D., Strukov, D.B., and Lanza, M. (2020). Wafer-scale integration of two-dimensional materials in high-density memristive crossbar arrays for artificial neural networks. Nature Electronics *3*, 638–645. URL: https://doi.org/10.1038/s41928-020-00473-w. doi: 10.1038/s41928-020-00473-w.

89. Lee, H.J., Kim, J.H., Kim, H.J., and Lee, S.N. (2024). Improvements in Resistive and Capacitive Switching Behaviors in Ga_2O_3 Memristors via High-Temperature Annealing Process. Materials *17*, 2727. doi: 10.3390/ma17112727.

90. Islam, M.S., Lee, J., Ganguli, S., and Roy, A.K. (2023). Effect of oxygen vacancy and si doping on the electrical properties of Ta_2O_5 in memristor characteristics. Scientific Reports *13*, 16656. doi: 10.1038/s41598-023-43888-z.

91. Chen, J., Xiao, M., Chen, Z., Khan, S., Ghosh, S., Macadam, N., Chen, Z., Zhou, B., Yun, G., Wilk, K., Psaltakis, G., Tian, F., Fairclough, S., Xu, Y., Oliver, R., and Hasan, T. (2025). Inkjet-printed reconfigurable and recyclable memristors on paper. InfoMat *n/a*, e70000. doi: 10.1002/inf2.70000.